

## Accepted Manuscript

Retrieving shallow shear-wave velocity profiles from 2D seismic-reflection data with severely aliased surface waves

L.E. Onnis, A. Osella, J.M. Carcione



PII: S0926-9851(18)30254-4  
DOI: <https://doi.org/10.1016/j.jappgeo.2018.11.014>  
Reference: APPGEO 3665  
To appear in: *Journal of Applied Geophysics*  
Received date: 23 March 2018  
Revised date: 16 November 2018  
Accepted date: 18 November 2018

Please cite this article as: L.E. Onnis, A. Osella, J.M. Carcione , Retrieving shallow shear-wave velocity profiles from 2D seismic-reflection data with severely aliased surface waves. *Appgeo* (2018), <https://doi.org/10.1016/j.jappgeo.2018.11.014>

This is a PDF file of an unedited manuscript that has been accepted for publication. As a service to our customers we are providing this early version of the manuscript. The manuscript will undergo copyediting, typesetting, and review of the resulting proof before it is published in its final form. Please note that during the production process errors may be discovered which could affect the content, and all legal disclaimers that apply to the journal pertain.

Retrieving shallow shear-wave velocity profiles from 2D seismic-reflection data with  
severely aliased surface waves

Omnis, L. E<sup>a,b,\*</sup>, Osella, A<sup>a,b</sup> and Carcione, J. M<sup>c</sup>

leomis@df.uba.ar<sup>\*</sup>, osella@df.uba.ar, jcarcione@inogs.it

<sup>a</sup>Universidad de Buenos Aires. Facultad de Ciencias Exactas y Naturales. Departamento de Física. Buenos Aires, Argentina.

Intendente Güiraldes 2160, Ciudad Universitaria, Pabellón I, Buenos Aires, Argentina.

<sup>b</sup>CONICET. Universidad de Buenos Aires. Instituto de Física de Buenos Aires (IFIBA). Buenos Aires, Argentina.

Intendente Güiraldes 2160, Ciudad Universitaria, Pabellón I, Buenos Aires, Argentina.

<sup>c</sup>Istituto Nazionale di Oceanografia e di Geofisica Sperimentale (OGS), Trieste, Italy.

Borgo Grotta Gigante 42C, 34010 Sgonico, Trieste, Italy.

\*Corresponding author.

*Expected widths for the figures are indicated in their captions. Color is not needed for any in print.*

**Abstract**

The inversion of surface-wave phase-velocity dispersion curves provides a reliable method to derive near-surface shear-wave velocity profiles. In this work, we invert phase-velocity dispersion curves estimated from 2D seismic-reflection data. These data cannot be used to image the first 50 m with seismic-reflection processing techniques due to the presence of indistinct first breaks and significant NMO-stretching of the shallow reflections. A surface-wave analysis was proposed to derive information about the near surface in order to complement the seismic-reflection stacked sections, which are satisfactory for depths between 50 to 700 m. In order to perform the analysis, we had to overcome some problems, such as the short acquisition time and the large receiver spacing, which resulted in severe spatial aliasing. The analysis consists of spatial partitioning of each line in segments, picking of the phase-velocity dispersion curves for each segment in the  $f$ - $k$  domain, and inversion of the picked curves using the neighborhood algorithm. The spatial aliasing is successfully circumvented by continuously tracking the surface-wave modal curves in the  $f$ - $k$  domain. This enables us to sample the curves up to a frequency of 40 Hz, even though most components beyond 10 Hz are spatially aliased. The inverted 2D  $V_S$  sections feature smooth horizontal layers, and a sensitivity analysis yields a penetration depth of 20-25 m. The results suggest that long profiles may be more efficiently surveyed by using a large receiver separation and dealing with the spatial aliasing in the described way, rather than ensuring that no spatially aliased surface waves are acquired.

**Keywords:** surface waves, shear-wave velocity, spatial aliasing, MASW, Neighborhood Algorithm.

## 1. Introduction

The dispersion relation of seismic surface waves is mainly sensitive to variations in the shear-wave velocity ( $V_S$ ). The experimental determination of the group or phase-velocity dispersion curves, followed by a suitable inversion scheme, is a cost effective and nondestructive way to obtain reliable estimates of the shallow  $V_S$  structure. The spectral analysis of surface waves method (SASW) requires only two receivers deployed in different layouts, and has been extensively used, particularly for geotechnical applications (Nazarian and Stokoe, 1984). Moreover, the multichannel analysis of surface waves method (MASW) and similar array-based methods have become increasingly important (Park et al., 1999; Xia et al., 1999).

In a typical multichannel surface-wave survey, Rayleigh waves are recorded by a linear array of 24-48 or more vertical geophones using either active or passive sources, or a combination of both (e.g., Foti et al., 2018; Lontsi et al., 2016; Pamuk et al., 2017). Passive seismic data or microtremors are enriched in low-frequency (long wavelength) components that can significantly extend the depth of penetration. The phase-velocity dispersion curve determination is usually performed after a wavefield transform from the original  $x-t$  domain to a more convenient one in which the surface-wave dispersion curves are more easily picked. Extensively used transforms include the slowness-frequency (McMechan and Yedlin, 1981), phase-shift (Park et al., 1998), and frequency-wavenumber transforms (Yilmaz, 2001). Most surface-wave studies involve the determination and inversion of fundamental mode phase-velocity dispersion curves alone, because higher modes are more difficult to excite. If higher mode dispersion curves can be properly sampled, their joint inversion with the fundamental mode can constrain the inversion and increase the penetration depth. Even if not used, it is always important to recognize them to avoid interpretation errors.

The phase-velocity dispersion curve is then inverted under the assumption of a layered 1D medium. Further simplifications include assuming a given value for the density and Poisson's ratio, because the dependence of the dispersion curve on both density and longitudinal velocity is weaker than on  $V_S$  (Nazarian, 1984). The inversion is performed using either local or global search methods. Local methods are computationally inexpensive when compared to global methods, but require an initial model that might bias the results, and can lead to local minima. Global methods, such as simulated annealing (Metropolis et al., 1953), genetic algorithms (Sen and Stoffa, 2013) and the neighborhood algorithm (Sambridge, 1999), can provide more reliable results at the expense of increased computational resources. Each is governed by different input parameters that must be adjusted to control the search, and their efficiency scales differently with the parameter-space dimension (Sajeva et al., 2017).

When surface waves are recorded using multifold acquisition setups, either surface-wave surveys or as part of seismic reflection or refraction surveys, it is possible to obtain 2D laterally varying models by combining several 1D models. Xia et al. (2000) obtained a pseudo 2D model by applying MASW to different shot gathers with a roll-along moving-line acquisition geometry. Multifold data also enables stacking techniques that significantly enhance the data quality in the wavefield-transformed domain (Grandjean and Bitri, 2006; Neduczka, 2007).

Socco et al. (2010) highlighted the benefits of data integration between body wave and surface-wave methods, ranging from the simple comparison of the results to full-fledged joint inversion. They also indicate that properly designed surveys can enable both types of analysis for a single dataset. Strobbia et al. (2011) performed the analysis of surface waves on 3D seismic data to derive a near-surface model and used it to implement model-based attenuation schemes. 2D multifold data, including seismic-reflection data, has also been used to retrieve lateral variations in near-surface  $V_S$  models. Laterally smooth models have been obtained using a laterally constrained inversion strategy (Bergamo et al., 2012; Socco et al., 2009; Socco and Boiero, 2008) but also through laterally independent inversions based on global methods (Pasquet and Bodet, 2017).

In this work, we perform the analysis of surface waves recorded on four 2D seismic-reflection lines. They were acquired as part of a paleoenvironmental study of the Llancaño Lake basin, southern Mendoza Province, Argentina. In a preliminary study, Carcione et al. (2013) analyzed a common-shot gather and obtained a stacked section, showing that useful information can be extracted from surface and lateral waves. The seismic-reflection processing is described in detail by Osella et al. (2015) and the complete results are

given by Onnis et al. (2017). The maximum imaging depth is around 700 m, but certain data characteristics, including the lack of conspicuous first breaks and considerable NMO stretch of early events, made it difficult to obtain an adequate image of the shallow (<50 m) region through seismic-reflection processing techniques. The surface-wave analysis is intended to derive complementary near-surface information and also to make use of the surface-wave data which otherwise would be completely discarded.

Because the lines were originally acquired with only seismic-reflection processing in mind, the acquisition parameters are non-optimal for recording surface waves. The large receiver separation results in severe spatial aliasing, the acquisition time is not long enough to record them on far offset traces and there is poor receiver sensitivity in the low-frequency region. Overcoming these challenges requires the implementation of convenient strategies.

The analysis comprises the binning of data among several sites, the determination of modal phase-velocity dispersion curves in the  $f$ - $k$  domain for each site (using stacking techniques enabled by the data redundancy), and their independent inversion by means of the global inversion neighborhood algorithm. The resulting 1D shear-wave velocity models are then combined to build 2D  $V_S$  pseudosections.

## **2. Reflection survey**

The analyzed data consists of four seismic-reflection lines, each 950 m long and located along two East-West transects north of Llanquanelo Lake (Figure 1). The acquisition was performed with fixed-line geometry using a Geometrics Geode DZ system, 96 receivers with 10 m separation (10 Hz vertical geophones), and 4000 Hz sampling rate. Some acquisition parameters were line dependent. Lines 1 and 2 were acquired using a GISCO ESS 100 accelerated-weight source, activated in the midpoint of each consecutive receiver pair (every 10 m), with 1.8 s recording time and two-fold vertical stacking. For lines 3 and 4 the source was an Ambrogeo seismic rifle activated at the alternate midpoints of consecutive receiver pairs (every 20 m), with 0.8 seconds recording time and no vertical stacking.

There are also clear differences in the soil properties of each pair of lines. Lines 1 and 2 extend over piedmont deposits of various lithologies between sands and clays, while lines 3 and 4 are located in the northern margin of the Llanquanelo Lake “*salina*”, a salty coastal plain formed by water evaporation (de la Vega et al., 2012). These differences are *a priori* expected to translate into differences in seismic response, particularly at the near surface.

An inspection of the common shot gathers (an example is given in Figure 2) show many features which are common to a large majority of the shots, regardless of the line. These include high amplitude broadband ground roll, indistinct first breaks and poor reflection energy. The ground-roll is slow, with velocities no higher than 400 m/s and appreciable energy below 200 m/s. Conspicuous reflections are mostly restricted to near offsets (< 300 m) and early times (< 0.4 s), and are completely lost when overlapping the ground-roll noise cone. Most shots contain no more than one clear reflection, though many contain two or three possible ones. It is difficult to determine if very early events are refractions or reflections.

Pre-stack processing consists of frequency bandpass filtering, automatic gain control and mute of the noise cone. The lack of significant reflection energy on raw common-shot gathers persists on processed CMP gathers, and semblance analysis panels permit at most a single pick per CMP, linked to shallow reflections (< 0.1 s two-way travel time). On the other hand, line-wide constant velocity panels result in a single 1D velocity model for each line, but allow us to pick one or two additional reflections between 0.3 and 0.6 s. These reflections are only tentatively recognizable in the field records, but the resulting stacked sections show good lateral continuity with additional seismic-reflection profiles in the region, including oil industry data (Onnis et al., 2017). Thus, the inferred reflectors are regarded as real geological features. Figure 3 shows, as an example, the depth stack of line 1.

A detailed account of the seismic-reflection processing is given by Osella et al. (2015). However, aspects relevant to the subsequent surface-wave analysis will be emphasized here. Most important is the fact that the surface waves exhibit severe spatial aliasing. All lines contain significant surface-wave energy at velocities

lower than 200 m/s, and the Nyquist wavelength is 20 m, implying that components with frequency greater than 10 Hz will be spatially aliased. Frequency bandpass filtering shows that the reflection energy is concentrated in the 30-90 Hz range, so that the aliased surface waves are not separable from reflections in the  $f$ - $k$  domain. Figure 4 shows the  $f$ - $k$  spectra of a common shot gather illustrating this fact. As a consequence of the spatial aliasing, surface waves cannot be properly attenuated using multichannel filters such as those in the  $f$ - $k$  or  $\tau$ - $p$  domains. It was decided to suppress them completely by muting the entire noise cone. This effectively discards any information that overlapping reflections might contain.

Another important aspect is that no shallow ( $< 50$  m) subsurface information can be obtained. First breaks are indistinct and it is unfeasible to pick them reliably in order to derive a consistent near-surface velocity model. The lack of such a model precludes the computation of adequate static corrections. In our survey, all sources and receivers lie on an essentially flat surface, so elevation static corrections are not mandatory, but the near-surface model itself would be a valuable result. Additionally, the noise muting increases the relative importance of far-offset traces on the stacked sections, so that significant NMO-stretch effects are observed. The best results are obtained when applying severe stretch mutes, but either because of stretching or muting, the shallow subsurface is not adequately resolved in the stacked sections.

The data was originally acquired as part of a paleoenvironmental study, with the purpose of depicting stratigraphic sequences up to a depth of several hundred meters. Although the deeper results are satisfactory, the research could also benefit from shallow subsurface information. The surface-wave method was then proposed as a way to extract information from the muted surface waves, and use it to derive complementary information about the near-surface structure.

### **3. Surface-wave analysis**

The surface-wave analysis for each line consists of three steps. The first step consists in partitioning each seismic line in several overlapping receiver segments, and determining the shots for the analysis of each segment. In the second step, the  $f$ - $k$  amplitude spectra from all shots associated with a given segment are stacked, and frequency-slowness curves are picked for all surface-wave modes observed in each stacked spectra. Statistical errors are also estimated. Finally, each segment's curves are inverted by means of a 1D global optimization method, the neighborhood algorithm, and the resulting 1D  $V_S$  models are combined to obtain 2D pseudosections. The inversion also provides results for  $P$ -wave velocity and density profiles, but as the dependence of the phase-velocity dispersion curve on these properties is weak, such inversion is regarded as an ill posed problem.

#### **3.1 Spatial windowing of surface-wave data**

The partitioning of each line in several segments is intended to make the inversion 1D hypothesis plausible, and to permit the retrieval of lateral variations along the line. Beyond the fact that data is shared among different segments, the analysis for each segment can be performed independently. For the purpose of building 2D sections, the 1D  $V_S$  model obtained for a given segment is associated with a site at its center, because it is primarily determined by structures beneath the receiver array, rather than beneath the source (Luo et al., 2009).

For a given line, segments are built by moving a fixed length segment starting at a line end towards the other end, one receiver at a time. In this way each segment overlaps several others, and the resulting 1D model horizontal spacing equals the receiver interval. To take advantage of the multifold data, multiple shots are considered for each segment and a statistical treatment is performed. For each segment, shots from outside the segment are selected in accordance to the following maximum and minimum offset restrictions:

$$X_{MAX} < V_{SLOWEST} T \quad (1)$$

$$X_{MIN} > \lambda_{MAX} / 2 \quad (2)$$

where  $T$  is the time acquisition window,  $\lambda_{MAX}$  is the maximum wavelength,  $V_{SLOWEST}$  is the slowest velocity of the surface waves,  $X_{MIN}$  is the minimum source-to-first-receiver offset, and  $X_{MAX}$  is the maximum overall offset. Figure 5 shows these relevant distances.

Equation 1 indicates that only shots in which all surface waves reach all receivers are considered. This is due to the limited time window, and accounts for the fact that not all surface waves travel at the same speed. The condition of equation 2 constrains the so called near-field effects. Inversion algorithms assume plane-wave propagation, and near-offset traces are likely to exhibit cylindrical front effects, as well as increased body wave contamination. Near-field distortions are more noticeable in long-wavelength components, and the distance at which they can be considered negligible is model dependent. The chosen value is an optimistic estimate inferred from SASW studies (Sánchez-Salineró, 1987; Tokimatsu, 1995).

Values for  $V_{SLOWEST}$  and  $\lambda_{MAX}$  were preliminarily estimated from the visualization of  $f-k$  spectra, where the phase-velocity dispersion curve picking was performed. The first parameter that must be determined is the segment length. It needs to be short enough so that the 1D hypothesis is plausible, but long enough to allow adequate spectral resolution. The visualization of phase versus offset plots, picked from narrow frequency bandpass filtered traces, has been proposed to assess changes in dispersion relation (Strobbia and Foti, 2006). However, it requires considerable manual picking and phase unwrapping, both unreliable due to the aliasing. Instead, the segment length is selected after qualitative observations of the  $f-k$  spectra obtained for different lengths. It is then relevant to first describe how the  $f-k$  spectra computation and curve picking is carried out for an arbitrary segment length.

### **3.2 Spectral stacking and dispersion curve picking**

The  $f-k$  domain was chosen to pick the phase-velocity dispersion curves due the conspicuous nature of aliased components. Dal Moro et al. (2003) provide an example with moderate spatial aliasing in which the phase-shift velocity spectrum adequately separates aliased and non-aliased components (Park et al., 1998). However, in our data the aliasing is severe, and the aliased and non-aliased components proved more difficult to discriminate in the velocity spectrum.

A stacked  $f-k$  spectrum was obtained for each segment by means of a 2D Fast Fourier Transform. For every shot, the  $f-k$  amplitude spectrum corresponding to the segment traces was computed after Gauss windowing and zero-padding in the spatial dimension (in that order), to increase resolution and reduce spectral leakage effects. For a given segment, the number of samples in the window function was equal to the number of receivers. The windowed data was then zero-padded up to 200 spatial samples, thus increasing the nominal resolution in the  $k$  axis. To account for the sign difference in the velocity of shots from opposite sides of the segment, shots with negative velocities were mirrored spatially before computing their spectra. All single-shot spectra were then summed.

Figure 6a shows a spectra obtained in this manner for a segment in line 2. The black and white dashed lines indicate the fundamental and first excited Rayleigh phase-velocity dispersion curves respectively, identified on the basis of their minimum frequency and their overall velocities. Higher modes always have higher than zero minimum frequencies, and typically greater velocities. Upon reaching the Nyquist wavenumber ( $k_{Nyq} = 0.05 \text{ m}^{-1}$ ), surface waves become spatially aliased and wrap around the  $k$  axis. It is possible to perform the picking on such plots, by taking into account that the  $k$  value of the picks must be corrected by  $2 k_{Nyq}$  every time the curve crosses the Nyquist wavenumber. A more convenient method is to plot the amplitude spectrum next to itself, extending the  $k$  axis once for each crossing. Figure 6b has been obtained in this way. The modified  $k$  axis can then be used to perform the picking continuously without additional corrections. It must not be misunderstood as a way to obtain spatial sampling beyond the Nyquist wavenumber, but only as a graphical method to automatically correct the wavenumber values of those components whose degree of aliasing is known.

The implemented stacking strategy significantly improves the surface waves SNR (signal-to-noise ratio), and results in smooth, interpretable  $f-k$  spectra in which modal curves can be identified, even for segments whose single-shot spectra are very noisy and difficult to interpret. The most significant improvement is in

the low-frequency region, where the receiver sensitivity is diminished. Figure 7 shows three single-shot spectra from a segment in line 2, and the improvement produced by increasing the stack fold.

The phase-velocity dispersion curve picking for each spectrum is carried out semiautomatically. Amplitude peaks along each frequency are computed and their positions are superimposed on the spectrum plot. We then manually select those peaks interpreted as modal curves. To select a definite segment length, stacked  $f-k$  spectra including peaks are represented for every segment, using lengths ranging from two receivers up the maximum possible number for which there are suitable shots in agreement with equations 1 and 2.

For each seismic line, the largest possible length that results in well-resolved spectra and coherent peak patterns is selected. The shorter segments always result in poorly resolved spectra, but the longer ones do not guarantee good resolution. Long segments have fewer shots contributing to the stack, and nominal spectral resolution gains are partially compensated by the decrease in SNR due to reduced stack fold. Also, the longer the segment, the less plausible the 1D hypothesis is. If strong lateral variations occur, spectra of shots from opposite ends of each segment will be dominated by different modal curve patterns which do not interfere constructively when stacked. In several cases, two very well differentiated patterns are superimposed on the same spectra, suggesting a step-like change in the elastic properties somewhere along the segment. Figure 8a shows an example featuring a branch in the fundamental mode pattern. When the segment is divided in two shorter non-overlapping ones, the independent and interpretable patterns of figures 8b and 8c, are obtained. Whenever long segments result in poorly resolved or very noisy spectra, strong lateral variations are suspected. The definitive segment length selected for each line is the one that maximizes the number of sites for which there are interpretable stacked spectra, suitable for picking the phase-velocity dispersion curves. It was selected as 110 m for lines 1 and 2, 50 m for line 3 and 40 m for line 4.

Once a segment length is chosen, preliminary picks for  $V_{SLOWEST}$  and  $\lambda_{MAX}$  are reassessed, and a single definitive line-wide value is estimated for each. Phase-velocity dispersion curves are then picked from the stacked spectrum of each segment across the entire line.

There are several noticeable differences in the spectra of the two western lines when compared to the two eastern lines. Most importantly, in lines 1 and 2 there are two clearly visible patterns interpreted as the fundamental and first higher mode spectral components. In these lines, coherent peak patterns extend into the low-frequency region, with fundamental mode frequency picks as low as 5 Hz. The sampling of seismic signals at frequencies lower than the geophones' natural frequency is commonly disregarded, because of the diminishing amplitude response. However, it has been shown that if the signals contain sufficient low-frequency energy, phase-velocity dispersion curves can be adequately sampled at frequencies an octave and a half below the geophones' natural frequency (Ivanov et al., 2008), and even lower (Rosa-Cintas et al., 2013). Given that most spectra from lines 1 and 2 exhibit well-resolved fundamental mode signals in the 5-10 Hz range, and these are consistently observed when moving from one segment to the next, we decided to perform the picking in this range.

In lines 3 and 4, a single pattern is observed. It is interpreted as the fundamental mode, and barely identifiable below 10 Hz. Figure 9 shows examples of good quality spectra from line 1 and line 3. The differences are likely to arise due to variations in the local near-surface environment, but also due to different acquisition parameters. Lines 1 and 2 have a larger time acquisition window and twice as many shot positions. Even taking into account the difference in segment length, this results in a larger stack fold (~12) when compared to that of lines 3 and 4 (~6). Therefore, lines 1 and 2 have smoother, more regular peak patterns on their spectra, which are interpretable for all segments. Approximately 10% of the segments from line 3 had to be discarded, while for line 4 several consecutive segments at each end of the line have very noisy spectra, and only segments between 350 and 650 m afforded suitable curves.

Actual picking is carried out by computing peaks in more frequency samples than shown on figures 8 and 9, with a 0.1 Hz frequency step. A slowness value is derived for each  $f-k$  pick. The frequency-slowness curves are then resampled with logarithmic distribution in frequency and reduced number of samples (~50) to obtain the definitive versions which are input to the inversion algorithm. The pick error for each line is

estimated by selecting three segments and performing the picking on their single shot spectra for all eligible shots. The upper bound of slowness standard error (across all three segments and frequency samples) is taken as the global slowness picking error for that line. As mentioned earlier, there are single shot spectra in which phase-velocity dispersion curve patterns are difficult to identify. In those cases the picks are performed using the stacked spectra for guidance.

To evaluate the quality and consistency of the picks, phase-velocity pseudosections are computed for each seismic line (Pasquet and Bodet, 2017; Strobbia et al., 2011). These are obtained by resampling the picked phase-velocity dispersion curves with regular spacing in wavelength, and representing the results as 2D sections in which the horizontal axis indicates the segment center, the vertical axis corresponds to the wavelength and the color indicates the phase velocity.

Figures 10 to 12 show the pseudosections obtained for all seismic lines and modes. All picked curves are sampled below 10 m, while the shortest wavelength that could have been sampled without the aliased components is 20 m. Line 1 results are the smoothest for both modes, and the fundamental mode picks have the longest maximum wavelengths. For line 2, there is an increase in the maximum sampled wavelength towards the east which correlates with an increase in the shear-wave velocity, and a noticeable gap around 600 m is observed for both modes. Lines 3 and 4 also show mainly smooth results, but with significant variability in the maximum wavelength, which is shorter compared to the other two lines.

### **3.3 Dispersion curve inversion**

Having set the segment length, it is unambiguous to refer to each segment by the value of its center coordinate, or site. The inversion of the phase-velocity dispersion curve for each site was carried out by using the Dinver open source package (Wathelet, 2008; Wathelet et al., 2004), which implements the Neighborhood Algorithm, a global search method (Sambridge, 1999a).

The method searches for the model (within a given parameter space) that minimizes the misfit function, defined as the RMS error-weighted discrepancy between modeled and target phase-slowness dispersion curves. Forward modeling is done by following Dunkin (1965). In the first step,  $N_0$  initial models are randomly sampled with uniform probability across the parameter space. In the second step,  $N_S$  models are generated by sampling with uniform probability but only inside the Voronoi cells of the  $N_R$  best-fitting models. For a given model, its Voronoi cell is the region of the parameter space in which all points are closer to it than to any other sampled model. Distances are measured by a non-dimensionalized  $L_2$  norm which depends on the parameter space. The second step is repeated  $N_{It}$  times.

The entire search strategy depends on four integer numbers and the parameter space. For a given total number of models ( $N_0 + N_{It} \times N_S$ ), higher  $N_S/N_R$  ratios and  $N_R \ll N_0$  indicate that at every step the search is focused towards the neighborhoods of a small fraction of models, while lower  $N_S/N_R$  ratios and  $N_R \sim N_0$  values imply a more exploratory search. Sambridge (2001) provides a semiempirical threshold total number of sampled models ( $d^{3.5}$ , with  $d$  the parameter space dimension) to distinguish between oversampled and undersampled regimes. For the oversampled case, a more exploratory strategy is recommended, while for undersampled searches, additional steps and a modified misfit function are prescribed. For simplicity, we restrict to oversampled searches, always exceeding the threshold number of models by at least a factor of two.

The method provides not only a best-fitting model, but rather an ensemble of all sampled models and their associated misfits. This enables a statistical estimation of the model error. All models for which the misfit is less than 1 are sampled at regular depth intervals, and the standard deviation of all  $V_S$  results at a given depth is computed to obtain a depth-dependent error estimate.

Regarding the parameter space, a layered media is considered, with each layer characterized by its  $S$ -wave and  $P$ -wave velocities, its density and its maximum depth (except the halfspace, for which the maximum depth is infinite). No a priori information was used to define the parameter ranges. The seismic-reflection velocity analysis fails to provide constraints to the acoustic velocities at shallow depths. Thus, conservative

(large) parameter ranges were considered preliminarily, with a maximum depth of up to 50 m and seismic velocities of up to 6000 m/s for all layers. Both were reduced after subsequent tests. No constraints were imposed upon their individual thicknesses. Allowed velocities are  $50 \text{ m/s} < V_S < 2000 \text{ m/s}$ ,  $100 \text{ m/s} < V_P < 3000 \text{ m/s}$ . If they result in a Poisson's ratio  $< 0.1$  the model is discarded without further computation. The density can vary between 800 and 3000  $\text{kg/m}^3$  but the same value is forced for all layers.

To determine adequate values of the number of layers and the search coefficients, a series of preliminary inversions is performed. The number of layers is varied between 2 and 7 (including the halfspace), while the search coefficients are always selected for maximum exploration ( $N_S=N_R=N_\theta$ ), but the actual values are varied, as well as the number of iterations.

Several guidelines can be obtained from these preliminary tests. The best-fitting results were obtained using large  $N_{It}$  ( $> 500$ ) and small  $N_S$  values rather than the opposite. In terms of minimum misfit, there are no significant benefits in sampling more models than twice the oversampling threshold number, nor in considering more than 5 layers. Additionally, laterally consistent results always feature a monotonic increase of velocity with depth. Whenever the best-fitting model of a site featured significant velocity inversion, it was not consistent with neighboring sites.

To determine whether a velocity inversion can actually be found by our choice of parameters, several synthetic models derived from the preliminary results but modified to feature a velocity inversion are considered. The phase-slowness curves for the fundamental mode of each model is computed, sampled at the same frequencies and with the same error as the experimental ones, and inverted using the same search coefficients and parameterization as during preliminary testing. In this manner, the velocity inversion is successfully retrieved for all synthetic models.

Additional tests with synthetic models were also carried out to assess the penetration depth. In this case, the modified models feature a halfspace with a  $V_S$  contrast comparable to largest observed on the preliminary results, and starting at increasing depths. The forward-computed phase-velocity dispersion curves are again inverted with sampling and error in accordance with the field data. Both 5 Hz and 10 Hz minimum frequency values were considered, and the fundamental mode was inverted independently as well as jointly with the first higher mode. The contrast was successfully retrieved up to 25 m for the 5 Hz inversions and 20 m for the 10 Hz, regardless of whether one or both modes were considered.

#### **4. Results**

For all four lines, the definitive inversion was performed by using a 5 layer parameter space with no velocity inversions allowed. Maximum allowed depth was 25 m for lines 1 and 2, and 20 m for lines 3 and 4. The definitive search parameters were  $N_S=N_R=N_\theta=50$  and  $N_{It}=800$ , thus sampling 40050 models in every inversion. Figure 13 provides an example of a 1D inversion result obtained using these parameters. It corresponds to the joint inversion of the fundamental and first higher modes, for a segment from line 2 centered at  $X=185 \text{ m}$ . Figure 13a shows the  $V_S$  profiles for the 30000 best-fitting models, while figures 13b and 13c shows the actual fit of the dispersion curves for both modes.

For lines 1 and 2, the fundamental mode was inverted independently and also jointly with the first higher mode. In all cases, 2D  $V_S$  sections were obtained from the 1D  $V_S$  profiles of the best-fitting models for each site. Figures 14 and 15 show the 2D sections corresponding to the fundamental mode inversion for all lines, while Figure 16 shows the results from the joint inversion of both modes, for lines 1 and 2. For a given site, depths beyond which the standard deviation of  $V_S$  values among eligible (misfit  $< 1$ ) models becomes large ( $> 20\%$ ) are omitted. At sites of line 3 for which no curves were picked, lateral interpolation was performed.

All lines feature nearly horizontal layers, with the top layer having a shear-wave velocity between 120 and 150 m/s. Its thickness increases from 2-3 m on the eastern lines to 6-7 m on the western lines. The second layer has velocities of approximately 350 m/s on lines 1 and 2, and 250 m/s on lines 3 and 4. On line 3 it is possible to assess its thickness of 4-5 m, as its bottom is resolved. On lines 1 and 2 it extends beyond the

research depth and on line 4 it is truncated due to significant dispersion beneath 10 m. Only on line 3 a third layer can be distinguished, with velocities of approximately 450 m/s.

For lines 1 and 2, the inclusion of the first higher mode produces mainly the same result, although with a smoother second layer and reduced dispersion in line 1. For line 2, a thin intermediate layer appears between the layers obtained in the single mode inversion (western half of the line). All sections exhibit a small number of isolated high-velocity results at depths below 10 m (i.e. around  $X=50$  m on line 3, or around  $X=450$  m on line 1, for the fundamental mode inversion case). These should be regarded as outliers resulting from the stochastic inversion, because their location was not consistent during the preliminary inversion runs. This inconsistency can also be observed in the definitive results of lines 1 and 2, when comparing both inversion schemes.

Even with its reduced length and truncated depth, results for line 4 are consistent with those from line 3 and constitute complementary information to the seismic-reflection profile.

## **5. Discussion**

All four sections have smooth lateral variations, which is remarkable given that each site's curves were inverted independently, without lateral constraints. Bias towards lateral smoothness is introduced by the fact that consecutive sites share all but two receivers, and most of the eligible source positions. Pasquet and Bodet (2017) actually recommend large overlaps to obtain smoothly varying models. However, the small lateral variations cannot be ascribed only to the overlap because sites separated by more than twice the segment length have no common traces. This distance is approximately 200 m for lines 1 and 2, and 100 m for lines 3 and 4, and no significant changes are observable in such scales. This suggests that smooth variations are an actual feature of the near-surface  $V_S$  structure.

The estimation of model  $V_S$  error through the standard deviation among eligible models is susceptible to bias. If a much larger number of iterations is run, for example by increasing  $N_{It}$  an order of magnitude, the new samples will tend to concentrate around the best-fitting ones, and the overall standard deviation will decrease. Rigorous error estimates are provided by Sambridge (1999b). Nonetheless, valuable qualitative insight can be obtained using the standard deviation criteria, such as that significant portions of the line 4 results are not reliable, even if within the estimated research depth.

The inclusion of higher-order modes in the inversion scheme is regarded as providing a greater penetration and better resolution at increasing depths. However, in the investigated cases the effect of including the first higher mode in the inversion is unclear. It did not affect the penetration depth assessment, and results for lines 1 and 2 are qualitatively similar in both cases. Due to the strict oversampling regime, it is possible that the additional constraints imposed by the higher mode phase-velocity dispersion curve are not as significant as they could be on an undersampled search, because the acceptable model regions might already be sufficiently sampled on the basis of the fundamental mode curve only.

Though the identification of the fundamental and first higher modes was always unambiguous, it is possible to test its validity. For lines 1 and 2, the first higher mode was computed for each of the best-fitting 1D models resulting from inverting only the fundamental mode, and then superimposed on the  $f-k$  stacked spectra for each site. In all cases, the forward-computed curve coincides with the patterns used to pick the first higher mode (Figure 17). The procedure was also applied to the  $f-k$  spectra from lines 3 and 4, for which no first-higher mode phase-velocity dispersion curves had been picked. In this case, the forward-computed first higher mode dispersion curves were compared to uninterpreted peak patterns to ascertain whether they could correspond to modal dispersion curve signals, and none was found to coincide. Likewise, the forward-computed second higher mode dispersion curves were superimposed on the  $f-k$  spectra from all lines and segments, and no peak patterns matched them.

Though the most significant challenge *a priori* was the severe spatial aliasing, in practice the implemented stacking technique coupled with convenient plotting in  $f-k$  domain allowed the adequate picking of surface-wave components in the 5-40 Hz range. However, the same simple solutions could fail for equally aliased

modal curves with more complex geometries in  $f$ - $k$  domain. In our case, the fundamental and first higher mode phase-velocity dispersion curves run parallel to each other for the most part, and aliased components cross at relatively high frequencies.

A more important factor is the reduced acquisition time window, which limits the maximum segment length, and the  $f$ - $k$  stack fold. Also, the optimistic estimate for the minimum offset was chosen out of necessity, to avoid excessively short segments with poorly resolved spectra that would result of using more conservative estimates.

Despite these shortcomings, it was possible to adequately sample the aliased surface-wave components in the 5 Hz-40 Hz and use them to derive near-surface  $V_S$  models up to a depth of 25 m. Comparatively, to obtain non-aliased surface waves up to a frequency of 40 Hz, considering the 120 m/s lower bound to Rayleigh wave velocity, a minimum separation of 1.5 m is needed. This can be accomplished by splitting the original line in consecutive shorter ones, which would require approximately six times the fieldwork but would not achieve the same spectral resolution. Therefore, to survey a long line with a limited number of receivers, it may be more efficient to use a large receiver separation and deal with the spatial aliasing in the manner described in Section 3 than to use a shorter receiver separation to prevent it. The success of such a strategy will ultimately depend on the actual phase-velocity dispersion curves, which could be assessed in a preliminary test using a single short array. In our survey, even this two-step procedure would reduce the fieldwork by at least a factor of three.

## **6. Conclusions**

We have shown that by implementing an adequate workflow, the phase-velocity dispersion curves of surface waves recorded on 2D seismic-reflection lines can be satisfactorily sampled and inverted to derive 2D near-surface shear-wave velocity models, even if all the components above the geophone resonant frequency are spatially aliased. The implemented workflow circumvents the aliasing problem by continuously tracking the surface-wave components in the  $f$ - $k$  domain. The tracking is simplified by plotting the  $f$ - $k$  spectra next to itself each time the phase-velocity dispersion curve signals intersect the Nyquist wavenumber. Such plots require negligible additional effort compared to picking the dispersion curves of adequately sampled, non-spatially aliased surface waves.

The stacking of  $f$ - $k$  spectra enabled by the multifold data greatly improves their interpretation and makes the picking feasible for several cases in which no single-shot spectra are interpretable. Conversely, factors limiting the stack fold such as the reduced time window and increased source spacing have a large negative impact in data quality. Thus, even for spatially aliased surface waves, simply extending the time window so that all surface waves reach all receivers yields significant improvements. We recommend the use of such extended acquisition time window in any 2D seismic-reflection survey which might benefit from the integration with surface-wave analysis. A longer acquisition time window would: 1) directly improve temporal frequency resolution, 2) indirectly increase the wavenumber resolution by increasing the maximum segment length, 3) increase spectral SNR due to increased stack fold and 4) allow more conservative near offset limits, thus reducing near field distortions.

Satisfactory results have been obtained for two conspicuously different surface types, using two different sources, suggesting that additional surveys in different settings may also benefit from sampling spatially aliased surface-wave components. This includes any other 2D seismic-reflection surveys in which spatial aliasing might ensue from the conflicting optimal requirements of surface-wave and body-wave methods. However, surveys purposely designed for surface-wave analysis can also benefit, because if high frequency components can be properly sampled despite their spatial aliasing, receiver separation can be increased to acquire longer profiles with no significant additional fieldwork.

**Acknowledgements.**

This work was partially supported by a grant from Agencia Nacional de Promoción Científica y Tecnológica, PICT 2014/1613.

ACCEPTED MANUSCRIPT

**References**

- Bergamo, P., Boiero, D., Socco, L.V., 2012. Retrieving 2D structures from surface-wave data by means of space-varying spatial windowing. *GEOPHYSICS* 77, EN39-EN51. <https://doi.org/10.1190/geo2012-0031.1>
- Carcione, J.M., De La Vega, M., Gei, D., Osella, A., Picotti, S., Tassone, A., Poscolieri, M., 2013. Seismic characterization of the quaternary sediments at Llanquanelo-Lake area, Argentina. *J. Seism. Explor.* 22, 1–17.
- Dal Moro, G., Pipan, M., Forte, E., Finetti, I., 2003. Determination of Rayleigh wave dispersion curves for near surface applications in unconsolidated sediments. *SEG Tech. Progr. Expand. Abstr.* 1247–1250. <https://doi.org/10.1190/1.1817508>
- de la Vega, M., Lopez, E., Osella, A., Rovere, E.I., Violante, R.A., 2012. Quaternary volcanic-sedimentary sequences and evolution of the Llanquanelo Lake region (Southern Mendoza, Western Argentina) evidenced from geoelectric methods. *J. South Am. Earth Sci.* 40, 116–128. <https://doi.org/10.1016/j.jsames.2012.08.002>
- Dunkin, J.W., 1965. Computation of modal solutions in layered, elastic media at high frequencies. *Bull. Seismol. Soc. Am.* 55, 335–358.
- Foti, S., Hollender, F., Garofalo, F., Albarello, D., Asten, M., Bard, P.Y., Comina, C., Cornou, C., Cox, B., Di Giulio, G., Forbriger, T., Hayashi, K., Lunedei, E., Martin, A., Mercerat, D., Ohrnberger, M., Poggi, V., Renalier, F., Sicilia, D., Socco, V., 2018. Guidelines for the good practice of surface wave analysis: a product of the InterPACIFIC project. *Bull. Earthq. Eng.* 16, 2367–2420. <https://doi.org/10.1007/s10518-017-0206-7>
- Grandjean, G., Bitri, A., 2006. 2M-SASW: Multifold multichannel seismic inversion of local dispersion of Rayleigh waves in laterally heterogeneous subsurfaces: Application to the Super-Sauze earthflow, France. *Near Surf. Geophys.* 4, 367–375. <https://doi.org/10.3997/1873-0604.2006010>
- Ivanov, J., Miller, R.D., Tsoflias, G., 2008. Some Practical Aspects of MASW Analysis and Processing. *Symp. Appl. Geophys. to Eng. Environ. Probl.* 2008 1186–1198. <https://doi.org/10.4133/1.2963228>
- Lontsi, A.M., Ohrnberger, M., Kruger, F., 2016. Shear wave velocity profile estimation by integrated analysis of active and passive seismic data from small aperture arrays. *J. Appl. Geophys.* 130, 37–52. <https://doi.org/10.1016/j.jappgeo.2016.03.034>
- Luo, Y., Xia, J., Liu, J., Xu, Y., Liu, Q., 2009. Research on the middle-of-receiver-spread assumption of the MASW method. *Soil Dyn. Earthq. Eng.* 29, 71–79. <https://doi.org/10.1016/j.soildyn.2008.01.009>
- McMechan, G.A., Yedlin, M.J., 1981. Analysis of dispersive waves by wave field transformation. *GEOPHYSICS* 46, 869–874. <https://doi.org/10.1190/1.1441225>
- Metropolis, N., Rosenbluth, A.W., Rosenbluth, M.N., Teller, A.H., 1953. Equation of State Calculations by Fast Computing Machines. *J. Chem. Phys.* 21, 1087–1092. <https://doi.org/doi:10.1063/1.1699114>
- Nazarian, S., 1984. In situ determination of elastic moduli of soil deposits and pavement systems by spectral-analysis-of-surface-waves method. PhD Dissertation, The University of Texas, Austin.
- Nazarian, S., Stokoe II, K.H., 1984. In situ shear wave velocities from spectral analysis of surface waves., in: 8th Conference on Earthquake Engineering, San Francisco, CA, July 21-28; pp. 31–38.
- Neduczka, B., 2007. Stacking of surface waves. *Geophysics* 72, V51–V58. <https://doi.org/10.1190/1.2431635>
- Onnis, L., Violante, R.A., Osella, A., De la Vega, M., Tassone, A., López, E., 2017. Neogene-Quaternary seismic stratigraphy of the Llanquanelo Lake Basin, Mendoza, Argentina. *Andean Geol.* 45, 35. <https://doi.org/10.5027/andgeoV45n1-3026>
- Osella, A., Onnis, L., de la Vega, M., Tassone, A., Violante, R.A., Lippai, H., López, E., Rovere, E.I., 2015. Seismic reflection survey at Llanquanelo region (Mendoza, Argentina) and preliminary interpretation of Neogene stratigraphic features. *J. South Am. Earth Sci.* 60, 71–81. <https://doi.org/10.1016/j.jsames.2015.03.005>
- Pamuk, E., Akgün, M., Özdağ, Ö.C., Gonenç, T., 2017. 2D soil and engineering-seismic bedrock modeling of eastern part of Izmir inner bay/Turkey. *J. Appl. Geophys.* 137, 104–117. <https://doi.org/10.1016/j.jappgeo.2016.12.016>
- Park, C.B., Miller, R.D., Xia, J., 1999. Multichannel analysis of surface waves. *GEOPHYSICS* 64, 800–808. <https://doi.org/10.1190/1.1444590>
- Park, C.B., Miller, R.D., Xia, J., 1998. Imaging dispersion curves of surface waves on multi-channel record, in: *SEG Technical Program Expanded Abstracts 1998*. pp. 1377–1380. <https://doi.org/10.1190/1.1820161>
- Pasquet, S., Bodet, L., 2017. SWIP: An integrated workflow for surface-wave dispersion inversion and profiling. *GEOPHYSICS* 82, WB47-WB61. <https://doi.org/10.1190/geo2016-0625.1>
- Rosa-Cintas, S., Galiana-Merino, J.J., Rosa-Herranz, J., Molina, S., Giner-Caturla, J., 2013. Suitability of 10 Hz vertical geophones for seismic noise array measurements based on frequency-wavenumber and extended spatial autocorrelation analyses. *Geophys. Prospect.* 61, 183–198. <https://doi.org/10.1111/j.1365-2478.2012.01114.x>
- Sajeva, A., Aleardi, M., Galuzzi, B., Stucchi, E., Spadavecchia, E., Mazzotti, A., 2017. Comparing the performances of four stochastic optimisation methods using analytic objective functions, 1D elastic full-waveform inversion, and residual static computation. *Geophys. Prospect.* 65, 322–346. <https://doi.org/10.1111/1365-2478.12532>
- Sambridge, M., 2001. Finding acceptable models in nonlinear inverse problems using a neighbourhood algorithm. *Inverse Probl.* 17, 387–403. <https://doi.org/10.1088/0266-5611/17/3/302>
- Sambridge, M., 1999a. Geophysical inversion with a neighbourhood algorithm - I. Searching a parameter space. *Geophys. J. Int.* 138, 479–494. <https://doi.org/10.1046/j.1365-246X.1999.00876.x>

- Sambridge, M., 1999b. Geophysical inversion with a neighbourhood algorithm-II. Appraising the ensemble. *Geophys. J. Int.* 138, 727–746. <https://doi.org/10.1046/j.1365-246X.1999.00900.x>
- Sánchez-Salineró, I., 1987. Analytical investigation of seismic methods used for engineering applications. PhD Dissertation, The University of Texas, Austin.
- Sen, M.K., Stoffa, P.L., 2013. *Global Optimization Methods in Geophysical Inversion*, Global Optimization Methods in Geophysical Inversion, Second Edition. Cambridge University Press, Cambridge. <https://doi.org/10.1017/CBO9780511997570>
- Socco, L.V., Boiero, D., 2008. Improved Monte Carlo inversion of surface wave data. *Geophys. Prospect.* 56, 357–371. <https://doi.org/10.1111/j.1365-2478.2007.00678.x>
- Socco, L.V., Boiero, D., Foti, S., Piatti, C., 2010. Seismic body and surface wave data integration for near surface characterisation, in: 72nd European Association of Geoscientists and Engineers Conference and Exhibition Incorporating SPE EUROPEC 2010, Workshops. pp. 183–187.
- Socco, L.V., Boiero, D., Foti, S., Wisén, R., 2009. Laterally constrained inversion of ground roll from seismic reflection records. *GEOPHYSICS* 74, G35–G45. <https://doi.org/10.1190/1.3223636>
- Strobbia, C., Foti, S., 2006. Multi-offset phase analysis of surface wave data (MOPA). *J. Appl. Geophys.* 59, 300–313. <https://doi.org/10.1016/j.jappgeo.2005.10.009>
- Strobbia, C., Laake, A., Vermeer, P., Glushchenko, A., 2011. Surface waves: Use them then lose them. Surface-wave analysis, inversion and attenuation in land reflection seismic surveying. *Near Surf. Geophys.* 9, 503–513. <https://doi.org/10.3997/1873-0604.2011022>
- Tokimatsu, K., 1995. Geotechnical site characterization using surface waves, in: Proceedings of 1st International Conference on Earthquake Geotechnical Engineering, Vol. 3, Tokyo, Japan, November 14–16. pp. 1333–1368.
- Wathelet, M., 2008. An improved neighborhood algorithm: Parameter conditions and dynamic scaling. *Geophys. Res. Lett.* 35. <https://doi.org/10.1029/2008GL033256>
- Wathelet, M., Jongmans, D., Ohrnberger, M., 2004. Surface-wave inversion using a direct search algorithm and its application to ambient vibration measurements. *Near Surf. Geophys.* 2, 211–221. <https://doi.org/10.3997/1873-0604.2004018>
- Xia, J., Miller, R.D., Park, C.B., 1999. Estimation of near- surface shear- wave velocity by inversion of Rayleigh waves. *GEOPHYSICS* 64, 691–700. <https://doi.org/10.1190/1.1444578>
- Xia, J., Miller, R.D., Park, C.B., Ivanov, J., 2000. Construction of 2D vertical shear-wave velocity field by the multichannel analysis of surface wave technique, in: Proceedings of the Symposium on the Application of Geophysics to Engineering and Environmental Problems. pp. 1197–1206.
- Yilmaz, Ö., 2001. Seismic data analysis. *Soc. Explor. Geophys.* 10. <https://doi.org/10.1190/1.9781560801580>

Figure captions and size preferences

**Figure 1:** (a) Location of the survey site. (b) Satellite image of the northern Llanquanelo Lake basin, showing the location of the four seismic-reflection lines. Each line was acquired using 96 geophones and is 950 m long. Sentinel-2 (ESA) image courtesy of the U.S. Geological Survey. (2 columns)

**Figure 2:** Common shot gather for a midline shot from line 4. (1 column)

**Figure 3:** Depth stack section of line 1. The arrows indicate the continuous horizons picked during the constant velocity stack analysis. Shallow horizons must be regarded as potentially stacked refractions or NMO-stretch artifacts. (1 column)

**Figure 4:**  $f$ - $k$  spectrum of a line-tail shot gather from line 3. Notice how spatially aliased components wrap several times around the  $k$  axis upon reaching the Nyquist wavenumber ( $0.05 \text{ m}^{-1}$ ). (1 column)

**Figure 5:** Diagram of the spatial partitioning for three consecutive segments. Stars and triangles represent sources and receivers respectively. Only black source positions are considered for the analysis of each segment, formed by four black receivers. (1 column)

**Figure 6:** (a)  $f$ - $k$  stacked spectrum of a segment from line 1, exhibiting aliased modal curve patterns. (b) The same spectrum repeated next to itself with an artificially extended  $k$  axis. This allows to continuously track the aliased components. (1.5 columns)

**Figure 7:**  $f$ - $k$  spectra corresponding segment from line 2 and varying degrees of stack fold. Each spectrum has its own color scale. (a-c) Single-shot spectra. (d) Fold 2. (e) Fold 6. (f) Fold 12. (2 columns)

**Figure 8:** (a) Stacked spectrum from line 1 exhibiting an apparent branch, associated with an excessive segment length. (b), (c): Stacked spectra corresponding to each half of the same segment, in which the branching is not observed. White circles indicate amplitude peaks along fixed frequency values, which are used for picking the phase-velocity dispersion curves. (2 columns)

**Figure 9:** Stacked  $f$ - $k$  spectra for segments of different lines. Circles indicate amplitude peaks along fixed frequency values. (a) Spectrum from line 1. The dashed black and white polygons indicate the fundamental and first higher phase-velocity dispersion curve picks respectively. (b) Spectrum from line 3. The dashed black polygon indicates the fundamental mode dispersion curve picks. (1.5 columns)

**Figure 10:** Phase-velocity pseudosections corresponding to both modal curves picked on line 1. (2 columns)

**Figure 11:** Phase-velocity pseudosections corresponding to both modal curves picked on line 2. (2 columns)

**Figure 12:** Phase-velocity pseudosections corresponding to the fundamental mode curves picked on lines 3 and 4. White gaps on line 3 correspond to the centers of segments for which picking was unfeasible. (2 columns)

**Figure 13:** 1D inversion results for a 110 m segment centered at  $X=185 \text{ m}$  on line 2, corresponding to the joint inversion of the fundamental and first higher mode phase-velocity dispersion curves. Each graph shows the results for the 30000 best-fitting models, with the color indicating each model's misfit. (a) Shear-wave velocity. The black curve indicates the best-fitting model shear-wave velocity profile. (b) Forward modeled phase-slowness curves of the fundamental mode. (c) Forward modeled phase-slowness curves of the first higher mode. (2 columns)

**Figure 14:** 2D  $V_S$  sections of lines 1 and 2 built from the 1D  $V_S$  profiles corresponding to the best-fitting models, obtained by inverting only the fundamental mode phase-velocity dispersion curve for each site. (2 columns)

**Figure 15:** 2D  $V_S$  sections of lines 3 and 4 built from the 1D  $V_S$  profiles corresponding to the best-fitting models, obtained by inverting only the fundamental mode phase-velocity dispersion curve for each site. (2 columns)

**Figure 16:** 2D  $V_S$  sections of lines 1 and 2 built from the 1D  $V_S$  profiles corresponding to the best-fitting models, obtained by jointly inverting the fundamental and first higher mode phase-velocity dispersion curves for each site. (2 columns)

**Figure 17:** stacked  $f$ - $k$  spectrum corresponding to a site from line 2. The solid black line is the first higher mode curve computed from inverting only the fundamental mode phase-velocity dispersion curve, indicated by the black dashed polygon. (1 column)

## Highlights:

- Exploitation of seismic-reflection data with surface-wave methods
- Dispersion curves are determined for the fundamental and 1st higher Rayleigh modes
- Components with less than half of the Nyquist wavelength are consistently sampled
- Best parameterizations have an increase of shear-wave velocity with depth
- Inverted sections show smooth horizontal layers up to a depth of 25 m

ACCEPTED MANUSCRIPT

(a)



(b)

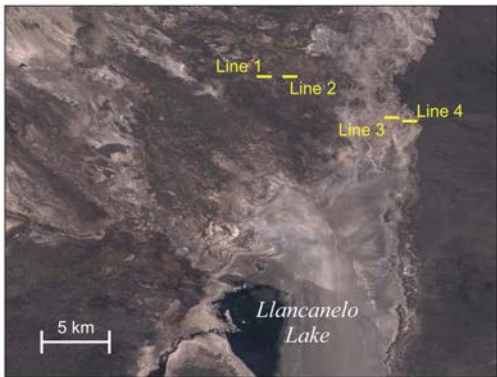


Figure 1

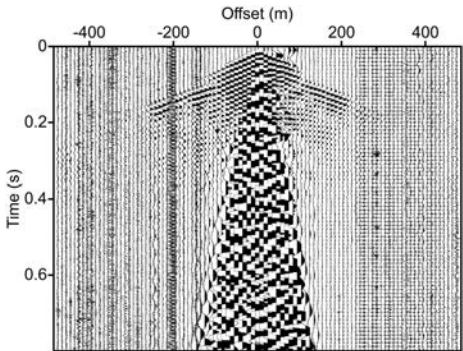


Figure 2

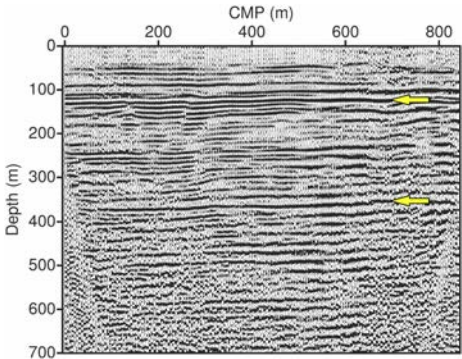


Figure 3

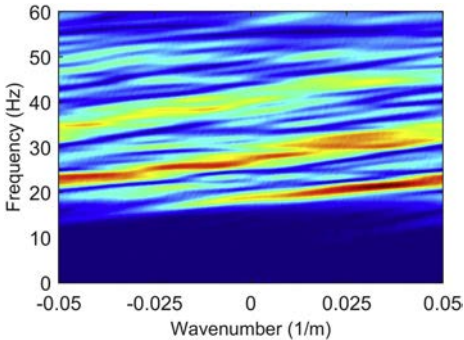


Figure 4

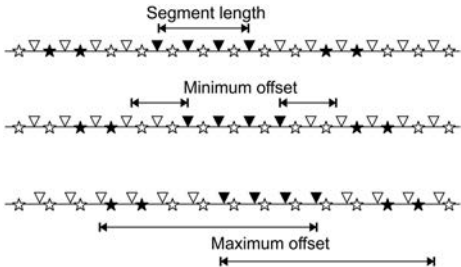
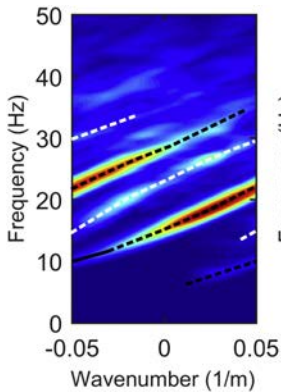
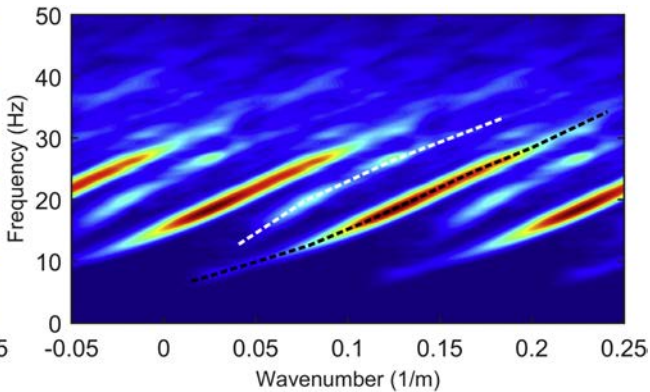


Figure 5



(a)



(b)

Figure 6

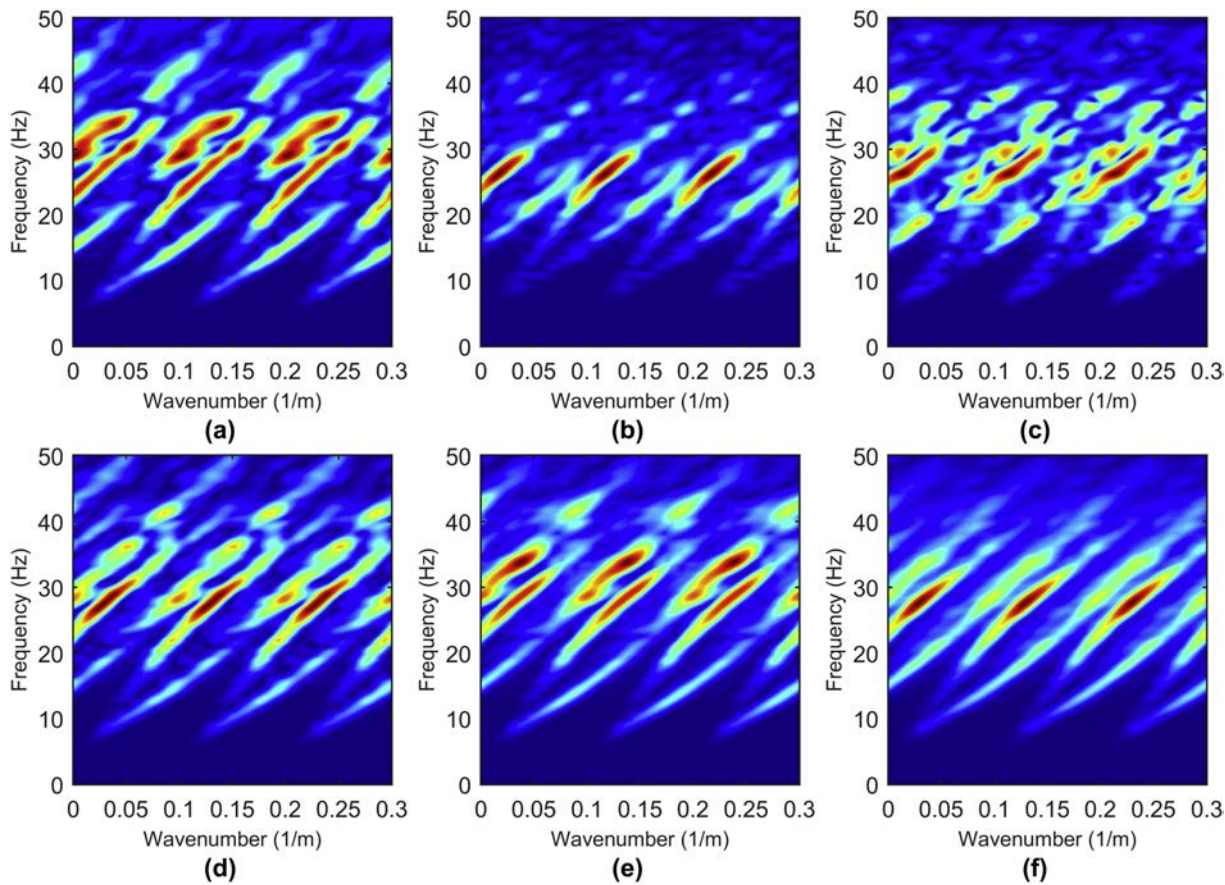


Figure 7

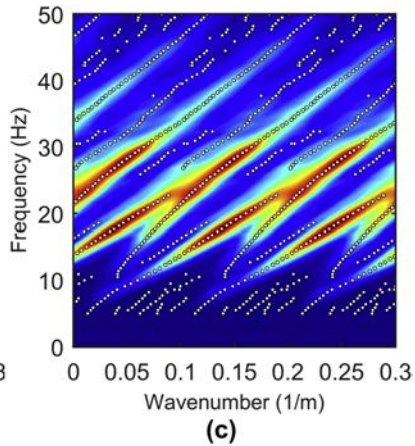
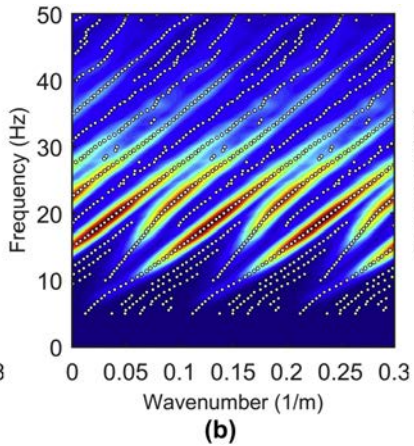
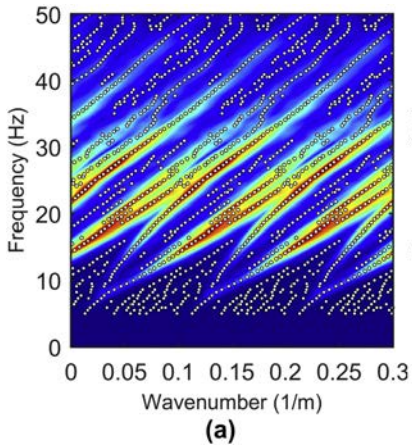


Figure 8

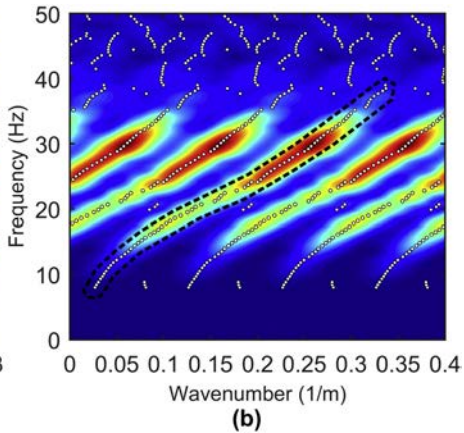
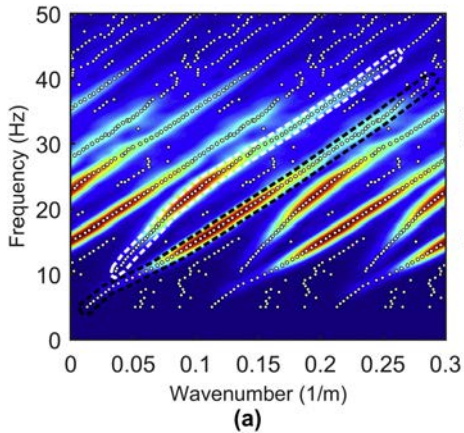
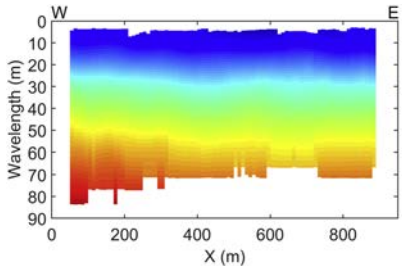
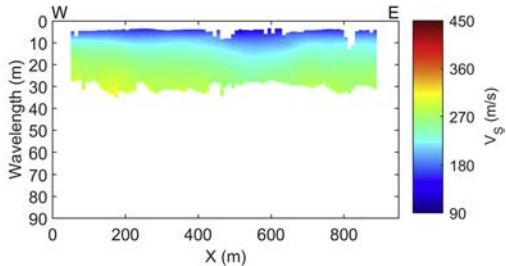


Figure 9

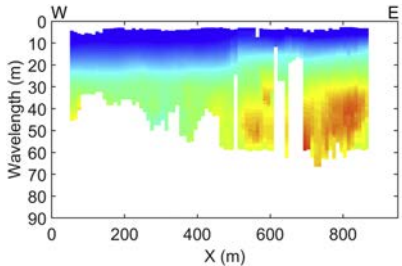


**Line 1: fundamental mode**

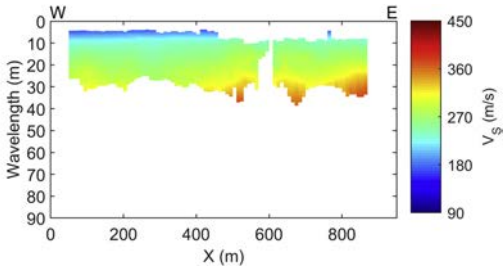


**Line 1: 1st higher mode**

Figure 10

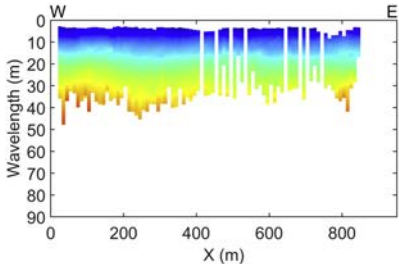


**Line 2: fundamental mode**

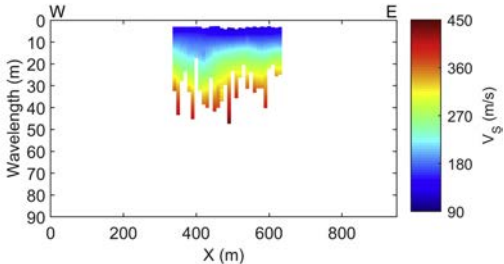


**Line 2: 1st higher mode**

Figure 11



**Line 3: fundamental mode**



**Line 4: fundamental mode**

Figure 12

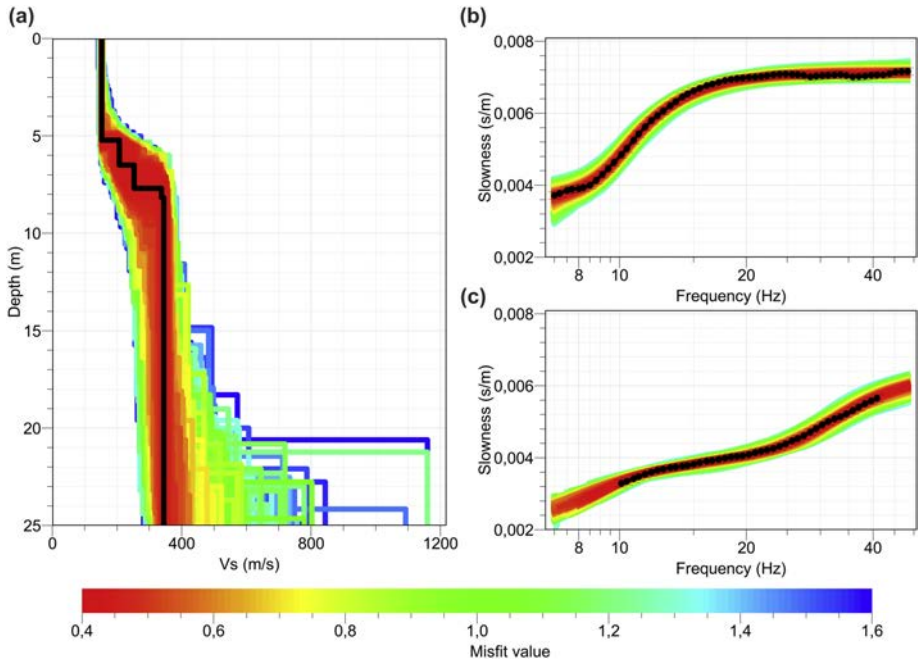


Figure 13

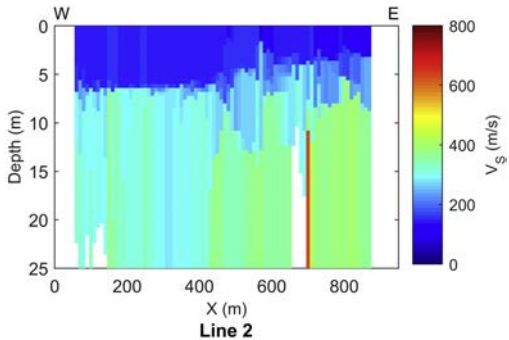
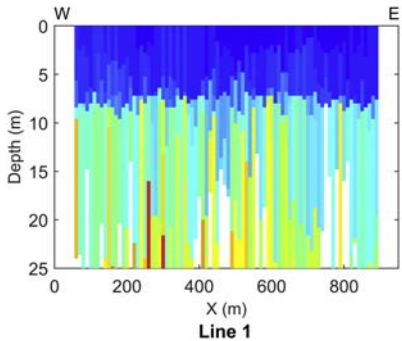


Figure 14

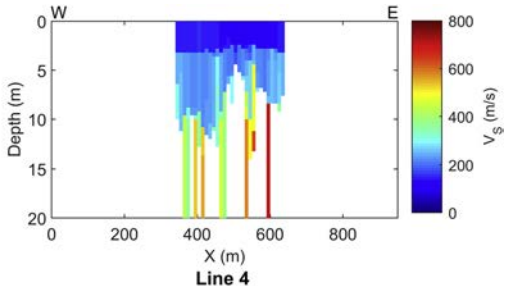
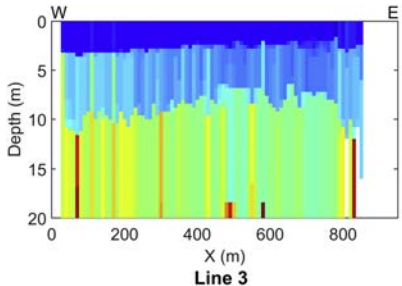


Figure 15

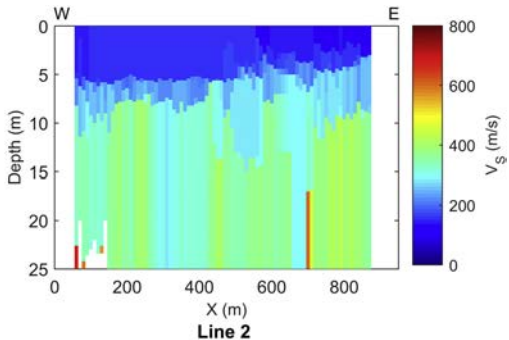
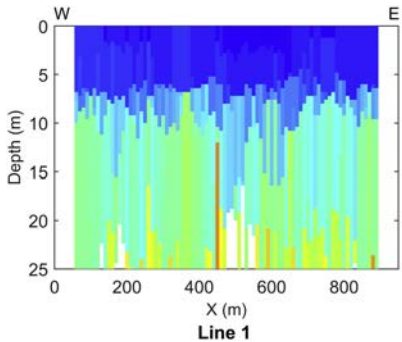


Figure 16

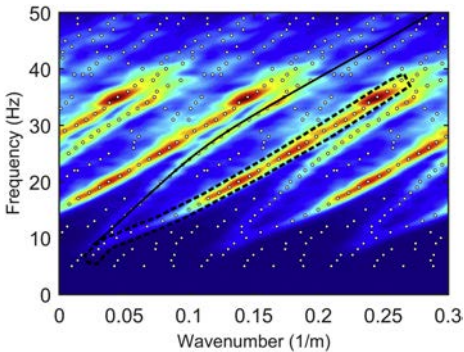


Figure 17